Decoupling between strain localisation and the microstructural record: evidence from in-situ strain measurements in polycrystalline ice

Marco A. Lopez-Sanchez*

Géosciences Montpellier – CNRS & Université de Montpellier, France
Present address: Dept. de Geología, Universidad de Oviedo, 33005, Oviedo, Spain

Thomas Chauve

Univ. Grenoble Alpes, CNRS, IGE, Grenoble, France

Maurine Montagnat

Univ. Grenoble Alpes, CNRS, IGE, Grenoble, France
Univ. Grenoble Alpes, Université de Toulouse, Météo-France, CNRS, CNRM, Centre d'Etudes de la Neige, Grenoble, France

Andrea Tommasi,

Géosciences Montpellier – CNRS & Université de Montpellier, France

**corresponding author: lopezmarco@uniovi.es*

Decoupling between strain localisation and the microstructural record: evidence from in-situ strain measurements in polycrystalline ice

Lopez-Sanchez, Marco A.[1,2,*], Chauve, Thomas[2], Montagnat, Maurine[2,4], Tommasi, Andréa[1]

[1]*Géosciences Montpellier – CNRS & Université de Montpellier, Montpellier, France*
[2]*Present address: Dept. de Geología, Universidad de Oviedo, 33005, Oviedo, Spain*
[3]*Univ. Grenoble Alpes, CNRS, IGE, Grenoble, France*
[4] *Univ. Grenoble Alpes, Université de Toulouse, Météo-France, CNRS, CNRM, Centre d'Etudes de la Neige, Grenoble, France*

**Corresponding author: e-mail: lopezmarco@uniovi.es*

Abstract

We explore the links between strain localization and the evolution of the microstructure in crystalline materials deforming by dislocation creep. Using digital image correlation (DIC), we monitored the evolution of the strain field in two coarse-grained columnar Ih ice samples deformed by creep (uniaxial compression at constant load) at −7 °C and 0.5 MPa up to 9.5% bulk shortening. After a brief transient (<0.2% bulk strain), in which strain localises nearby grain boundaries, viscoplastic strain concentrates in a few narrow intracrystalline shear bands that eventually extend over multiple grains. A comparison of pre and post-deformation crystal orientation maps shows that strain localisation in shear bands is mainly accommodated by basal glide without creating significant dislocation-related substructures. Severe dynamic recrystallization develops locally at grain boundaries that act as barriers to dislocation motion, especially where transfer of basal shear is ineffective. Full-field simulations reproducing the initial microstructure and experimental setup suggest that dynamic recrystallization is preferentially triggered at locations characterized by high work rates. Overall, these observations indicate that during the deformation of coarse-grained crystalline materials at high homologous temperatures: (1) recrystallization does not drive strain localisation but accommodates strain incompatibility and (2) large strains can be accommodated by unimpeded dislocation glide with no formation of dislocation substructures. Observation (2) implies that intragranular orientation gradients are unreliable gauges of viscoplastic strain intensity and that the proportion of dislocation types in subgrains does not gauge the relative contribution of different slip systems to deformation. These conclusions are extensible to all major rock-forming minerals, such as olivine and quartz, with important implications for the interpretation of microstructural data and models predicting the strain localisation as a function of microstructure evolution such as grain size reduction or dislocation distribution.

keywords: *Digital Image Correlation; Ice Ih; strain localisation; dynamic recrystallization; experimental deformation; viscoplastic anisotropy*

Highlights

- Ductile strain localisation may produce no clear microstructural record
- Deformation by single slip may produce no intragranular misorientation
- Intragranular orientation gradients do not gauge viscoplastic strain intensity
- Recrystallization mainly accommodates grain-scale strain incompatibility
- Transient strain localisation at most grain boundaries at strains <0.2%

1. Introduction

Variations in crystal orientation and viscoplastic anisotropy result in highly heterogeneous stress and strain rate fields during the deformation of polycrystalline materials like ice, rocks, or metallic alloys. The heterogeneity in the stress and strain rate fields controls the evolution of the microstructure, which in turn modifies the mechanical response of the polycrystal both at the local and larger scales. Understanding the complex feedbacks between the evolution of the microstructure and mechanical fields is essential to define accurate strain-dependent flow laws describing the mechanical behaviour of these materials. The links between the evolutions of the strain field at the polycrystal and grain scale and the microstructure (crystal orientations, grains sizes and shapes) can be unravelled through deformation experiments coupling technologies to measure both, preferably in situ. Digital image correlation (DIC) of random speckle patterns allows measuring displacement and strain fields at the microscale (Dong and Pan, 2017; Sutton et al., 2009), whereas the microstructure can be measured by optical or electron microscopy.

Due to its strong viscoplastic anisotropy, hexagonal (Ih) Ice is an ideal model material for probing the relations between local strain, intragranular misorientation, and dynamic recrystallization. Viscoplastic deformation in Ih ice crystals occurs essentially by the slip of dislocations with [1-120] Burger vectors on the basal plane (normal to the crystal [0001] or *c*-axis) (Duval et al., 1983; Weertman, 1983). Non-basal slip systems are at least 60 times harder to activate than the basal one (Duval et al., 1983). In polycrystals, however, there is indirect (Duval et al., 1983) and direct (EBSD-based) evidence for non-basal dislocations forming subgrains and representing up to ~35% of the observed geometrically necessary dislocations (Chauve et al. 2017; Weikusat et al. 2017). The large resolved shear stresses required to activate these slip systems imply local stress concentrations and high-stress heterogeneity within the polycrystal.

Previous deformation studies using DIC on Ih ice showed that the strain field is heterogeneous at both crystal and polycrystal scales. Uniaxial compression creep tests at -12°C, 0.5 MPa on columnar ice polycrystals documented strain localisation already in the transient creep stage (bulk strains ≤ 1%) (Grennerat et al., 2012). Strain localisation, with local strains five to ten times larger than the bulk strain, occurs in shear bands oriented at 30 to 60° to compression, with the highest strains nearby grain boundaries and triple junctions. Strain in individual grains does not correlate with the Schmid factor for the basal slip in the grain, hinting at a strong effect of grain interactions on the stress and strain distribution (Grennerat et al., 2012). DIC imaging of uniaxial compression creep tests in columnar ice at -7 and -10□C, 0.5 MPa to higher bulk strains highlighted a relationship between local strain and dynamic recrystallization, showing that nucleation was controlled by strong deformation gradients at triple junctions and boundaries between grains with markedly different orientations (Chauve et al., 2015; Piazolo et al., 2015). Grain-scale strain incompatibility also played an essential role in strain localisation at the brittle-plastic transition, where dynamic recrystallization and fracturing are coupled (Thomas Chauve et al., 2017).

In the present study, we focus on how grain interactions and activation of different deformation mechanisms, such as intracrystalline slip, dynamic recrystallization, and formation of kinks, affect strain localisation at the polycrystal scale at high homologous temperatures. We performed

compressional creep tests at high homologous temperatures up to 9.3% bulk shortening on Ih ice polycrystals composed of columnar centimetre-scale crystals. We tracked in situ using DIC the evolution of the viscoplastic deformation field at a resolution well below grain size (micrometric resolution) over the entire surface normal to both the compression direction and the columnar structure of the ice. We monitored the changes in the microstructure ex-situ by mapping crystal orientations on thin sections cut parallel and as close as possible to the face analysed by DIC before and after deformation. These two sets of observations are compared to the predictions of a full-field FFT-based model reproducing the experimental set-up and initial microstructure of the samples, but in which deformation occurs solely by dislocation glide.

2. Methods

We made polycrystalline columnar ice samples of 10×10×1.5 cm composed of ~ 65 to 75 columnar grains elongated normal to the square face of the sample, which is further referred to as the sample surface. The samples have thus a roughly 2D microstructure. The elaboration process is detailed in Grennerat et al. (2012). The area of the grain sections on the sample surface varies both within and among samples, but the grain sizes are mostly of centimetre scale (Figs 1 and 2). Grain boundaries lie nearly perpendicular to the sample surface in most cases. The large grain size favours dislocation creep relative to diffusion creep and grain boundary sliding. The sample initial microstructure facilitates the study of interactions between grains with different orientations and the detection of dynamically recrystallized grains. However, due to the limited number of grains, the samples are not representative volume elements and their mechanical response may be strongly conditioned by a few coarse grains at key positions in the aggregate, for example, the coarse grain that occupies more than half of the section in the central part of sample A (Fig. 1).

Samples were deformed in unconfined (room pressure) compression perpendicular to the columnar structure using an in-house dead-weight rig at -7 ºC (0.97 T_m, where T_m is the melting temperature) under initial uniaxial stress of 0.5 MPa up to 3.1 and 9.5 % bulk longitudinal shortening (Fig. 3a). Axial stress decreased slightly over time due to the increase in the cross-sectional area of the samples. For sample A (total bulk shortening of 3.1%) the final axial stress was 0.49 MPa, whereas for sample B (total bulk shortening of 9.5%) it was 0.48 MPa. Instantaneous strain rates during the experiments ranged from 3×10^{-7} to 9×10^{-7} s^{-1} (Fig. 3). Bulk strain (ε) and strain rates ($\dot{\varepsilon}$) was calculated by two different methods: (1) measuring the change in sample length ($l - l_0$) in the shortening direction directly on the image sequence following the displacement of the press trays and using $\varepsilon(\%) = 100 \times |(l - l_0) \div l_0|$, and (2) by averaging (median) over the full strain field estimated from digital image correlation in the shortening (y) direction.

For digital image correlation, a random speckle pattern was created on the sample surface by scratching-abrading the surface with sandpaper and then applying shoe polish with a brush to create high-contrast grey intensity gradients (for details on the procedure see Grennerat et al., 2012). The evolution of the displacement and the strain field during the experiments were measured using the free open-source Digital Image Correlation Engine (DICe) tool

(https://github.com/dicengine/dice) v2.0 from Sandia National Laboratories (Turner, 2015). Details on the methods and parameters used are provided in Table 1, Appendix A, and as metadata in the Supplementary material. Raw image resolutions were 17.26 μm/pixel (sample A) and 17.98 μm/pixel (sample B); detailed image acquisition setup and procedures are described in the Supplementary material. The optimal subset size was set at 35 × 35 pixels using the autocorrelation approach (Sutton et al., 2009). For an optimal result, step and virtual strain gauge (VSG) sizes were set at 12 (~1/3 of the subset size) and 24 pixels, respectively (International Digital Image Correlation Society et al., 2018). The step size corresponds physically to ~210 μm (VSG ~420 μm) and the maximum displacement resolution estimated was of ±6–7 μm for the x-direction (horizontal) and ±12–15 μm for the y-direction (vertical). The evolution of the strain field is presented as the Von Mises 2D equivalent strain ε_{eq} field

$$\varepsilon_{eq} = \sqrt{\frac{2}{3}\left(\varepsilon_{xx}^2 + \varepsilon_{yy}^2 + 2\varepsilon_{xy}^2\right)} \qquad (1)$$

The maximum equivalent strain resolution expected is $\pm 5.7\times10^{-4}$ (sample B) and $\pm 7.3\times10^{-4}$ (sample A), respectively. Strain field maps are presented as (1) incremental equivalent strain estimated over a 10 min creep interval normalized to the median equivalent strain, or as (2) finite (cumulative) equivalent strain. For reference, the bulk (longitudinal) shortening $\varepsilon(\%)$ is indicated in all strain field maps.

Table 1. Parameters and methods used to perform DIC (incremental)

Parameter/Method	Value
Initialization	feature matching
Optimization	gradient-based and simplex
Interpolation	keys cubic
Subset size	35 × 35 pixels (~612 × 612 μm)
Step size	12 pixels (~210 μm)
VSG size	24 × 24 pixels
Camera	Nikon D850 45.7 Mpx BSI CMOS sensor
Optics	Low-distortion Tamron SP Macro 1:1 lens
Image FOV	87-92 mm (height)
Image scale	~17.5 μm/pixel
Imaging rate	10 min
Exposure time	1/10 s

To characterize the evolution of the microstructure, we mapped the orientation of c-axes (azimuth θ and colatitude ϕ) before and after deformation on thin sections (~0.4 mm thick) cut parallel and as close as possible to the observation surface using the Automatic Ice Texture Analyser (AITA), which provides an angular resolution of ~3° (Peternell et al., 2011; Wilson et al., 2003). Pre- and post-deformation maps have spatial resolutions of 50 and 20 μm, respectively. Orientation data treatment, maps, and pole figures were made using the AITAToolbox (https://mecaiceige.gricad-pages.univ-grenoble-alpes.fr/tools/documentations/AITA-book/docs/intro.html).

As Ih ice deforms essentially by dislocation glide on the basal plane, the theoretical capacity of a grain to deform when subjected to axial compression can be approximated by the Schmid factor of the basal slip system using:

$$m_s = sin\phi\ sin\theta\ (\ 1 - sin^2\phi\ sin^2\theta)^{\frac{1}{2}} \quad (2)$$

A Schmid factor of 0.5 characterises grains with c-axes at 45° from the compression direction, leading to maximum resolved shear stresses on the basal plane, whereas a zero value implies c-axes parallel or perpendicular to the compression direction, leading to null resolved shear stresses on the basal plane. However, in strongly anisotropic polycrystals such as ice, the Schmid factor calculated using the macroscopic imposed stress is an unreliable measure of a crystal's ability to deform because grain interactions may produce local stresses that differ strongly in intensity and orientation relative to the macroscopic imposed stress (Grennerat et al., 2012). Comparison of the "macroscopic" Schmid factor with the actual strain of the grain provides therefore an estimate of the deviation of the local stresses relative to the macroscopic one.

Lastly, we performed full-field micro-macro simulations based on the pre-deformed microstructure of the samples using the CraFT code (Moulinec and Suquet, 1998). CraFT models crystal plasticity using an algorithm based on the discrete Fast Fourier Transform (FFT). It predicts the evolution of strain and stress fields in response to an imposed deformation for a prescribed crystal plasticity constitutive law and initial microstructure by minimizing the average local work rate under strain compatibility and stress equilibrium constraints. For simulating the deformation of Ice Ih, we used the elasto-viscoplastic law described in Suquet et al. (2012), which considers three slip systems: basal, prismatic, and pyramidal, strongly favouring basal slip. This constitutive law has been validated by comparison with experimental data at low strain (Grennerat et al., 2012; Piazolo et al., 2015). Since the simulation ignores changes in the microstructure (i.e. recrystallization) it can only reliably predict stress and strain fields before the development of recrystallization, i.e. below 0.5 to 1% bulk shortening (Chauve et al., 2015). Grain boundaries are represented as abrupt changes in crystal orientation without neither particular physical properties nor behaviour nor the possibility to slide or open. The undeformed microstructure of the sample surface was discretized at a 0.15 mm·pixel^{-1} step size giving respectively 533 × 600 (sample A) and 571 × 578 (sample B) Fourier points. Creep conditions equivalent to the experimental ones were applied up to a 1% bulk shortening, but the simulations have periodic boundary conditions, which differ from the stress-free lateral surfaces in the experimental setup. The effect of such an approximation was estimated by Grennerat et al. (2012) to be negligible, except on the very edges of the sample.

3. Results

3.1 Microstructural evolution

Sample A

Two coarse grains denoted as grains #1 and #2 in figure 1a characterise sample A. Grain #1, in the centre of the sample, had its basal planes at ~78° to the bulk compression direction. Grain #2, in the lower-left section of the sample, showed a notable intragranular orientation gradient with well-

defined subgrain boundaries delimiting domains with basal planes at 0° to 33° to the bulk compression direction. Both grains had low to moderate (0-0.25) initial Schmid factors indicating unfavourable crystal orientations to trigger basal slip in response to the imposed macroscopic stress (Fig 1d).

After a bulk shortening of 3.1%, grains #1 and #2 display markedly different microstructures. Grain #1 shows a notable change in shape but weak intragranular orientation gradients. Grain #2 shows less change in shape, but strong orientation gradients in the form of closely-spaced kink bands and subgrain boundaries (Figs. 1a, b, c). Most grain boundaries develop some degree of recrystallization, forming millimetre-sized grains along them (Fig. 1b, c), but severe dynamic recrystallization is limited to the boundary segment between grains #1 and #2 and the intersection of the shear band that crosscuts grain #1 with the neighbouring grain to the right (Fig. 1c, g).

Sample B

Sample B had a more homogeneous initial microstructure and a wider range of crystal orientations than sample A (Fig. 2). The upper right corner of sample B is composed of grains less than 1 cm wide, but more than 2/3 of the sample is composed of coarse columnar grains with fairly homogeneous sizes of a few cm (~3-6 grains across the sample height) (Fig. 2a). Most coarse grains had c-axes with intermediate colatitudes (angle to the imposed compression) and variable azimuths (Fig. 2a, e), resulting in moderate to high (>0.3) Schmid factors for basal glide (Fig. 2d). Sample B also had a few grains with c-axes oriented normal to the sample surface (dark hues in the orientation maps) and hence low Schmid factors (e.g., grain #2 in Fig. 2a).

After a bulk shortening of 9.5%, most coarse grains display an increase in the intragranular misorientation (Fig. 2b, c). As in sample A, the intragranular microstructure varies strongly between grains. For example, grains #1 and #6 show smooth and weak orientation gradients, whereas grains #4 and #7 display sharp orientation gradients delimited by kink bands and closely-spaced subgrains. The higher bulk shortening resulted in more extensive dynamic recrystallization than in sample A. Dynamic recrystallization developed mostly: (i) within grain #2 and its neighbours, (ii) along the boundary segment between grains #4 and #5, and (iii) to the right of grains #5 and #7 (Fig 2b, c). Comparison of crystal orientations before and after deformation reveals some dispersion of the original orientations due to intragranular distortion and recrystallization, but no major grain reorientations (Fig. 2e).

3.2 Macroscopic mechanical behaviour and the mean-field strain evolution from DIC

Sample A, shortened up to 3.1%, showed a primary creep stage characterized by a sharp decrease in the strain rate down to ~3×10^{-7} s^{-1} ~0.9 % bulk shortening. Then, the strain rate remained constant (steady-state) until the end of the experiment (Fig. 3a, b). The variation of the average (median) strain rate with time in the vertical direction (σ_{yy}) estimated from DIC follows a similar trend (Fig. 3b), validating the DIC strain field measurements up to 3.1%.

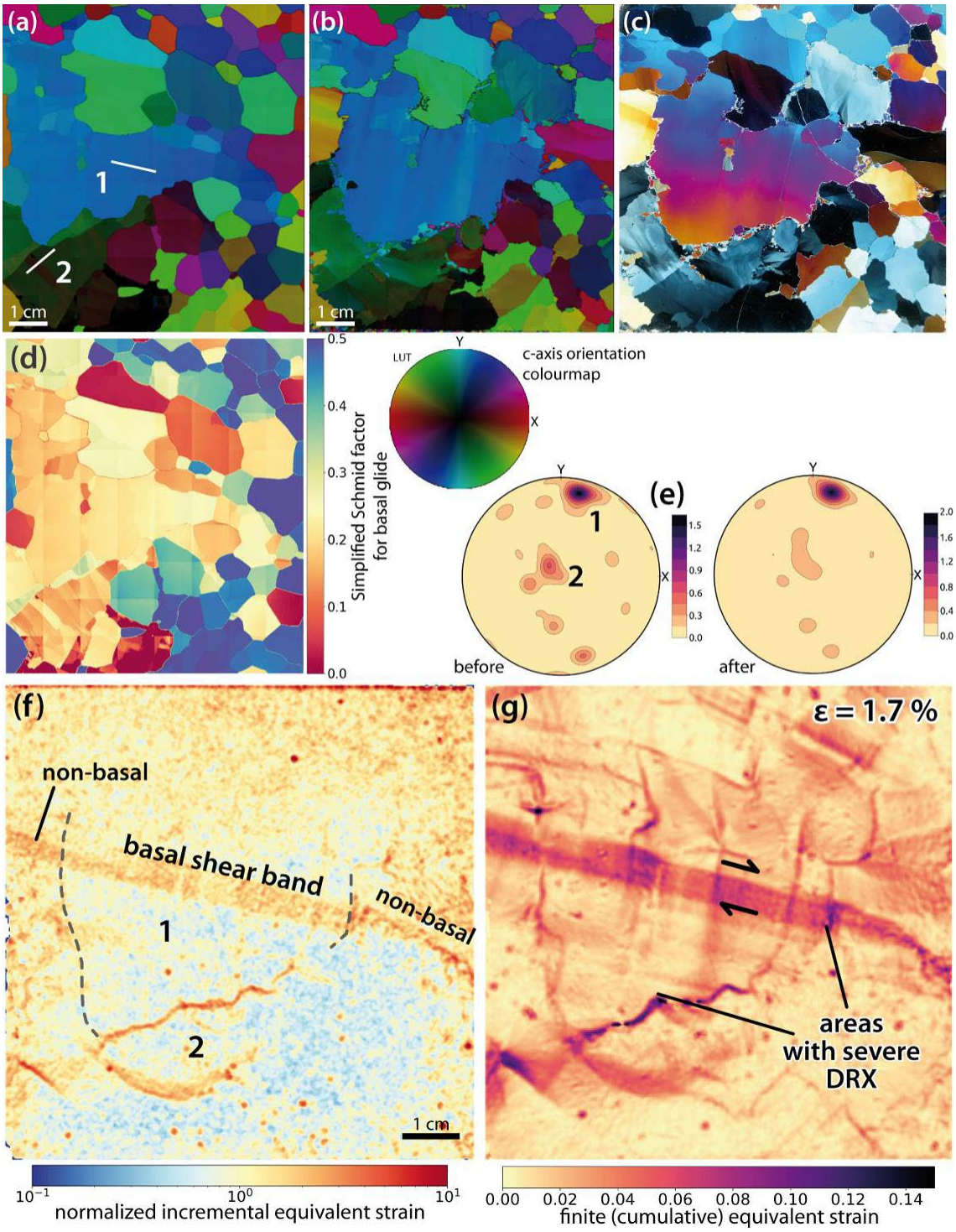

Figure 1. Microstructure, Schmid factor for basal glide, pre- and post-deformation CPO maps, and strain field at 1.7% bulk strain for sample A. (a, b) Pre- and post-deformation (3.1% bulk shortening) c-axis orientation maps. The projection of the basal planes onto the sample surface in the numbered grains is indicated by white lines in (a). (c) Post-deformation cross-polarized light image; the gentle colour gradient is due to a smooth change in thickness of the thin section. (d) Schmid factor map for basal glide according to initial crystal orientations. (e) Pre- and post-deformation contoured c-axis pole figures with orientations of

grains #1 and #2 indicated. Upper hemisphere equal-area projections. (f) Incremental Von Mises (2D) equivalent strain normalized to the median at 1.7% of bulk longitudinal strain. Blue and red areas are strained below and above the average respectively. Basal and non-basal shear bands are indicated. Incremental strain is estimated every 10 minutes of creep. (g) Finite (cumulative) Von Mises 2D equivalent strain at 1.7% of bulk strain.

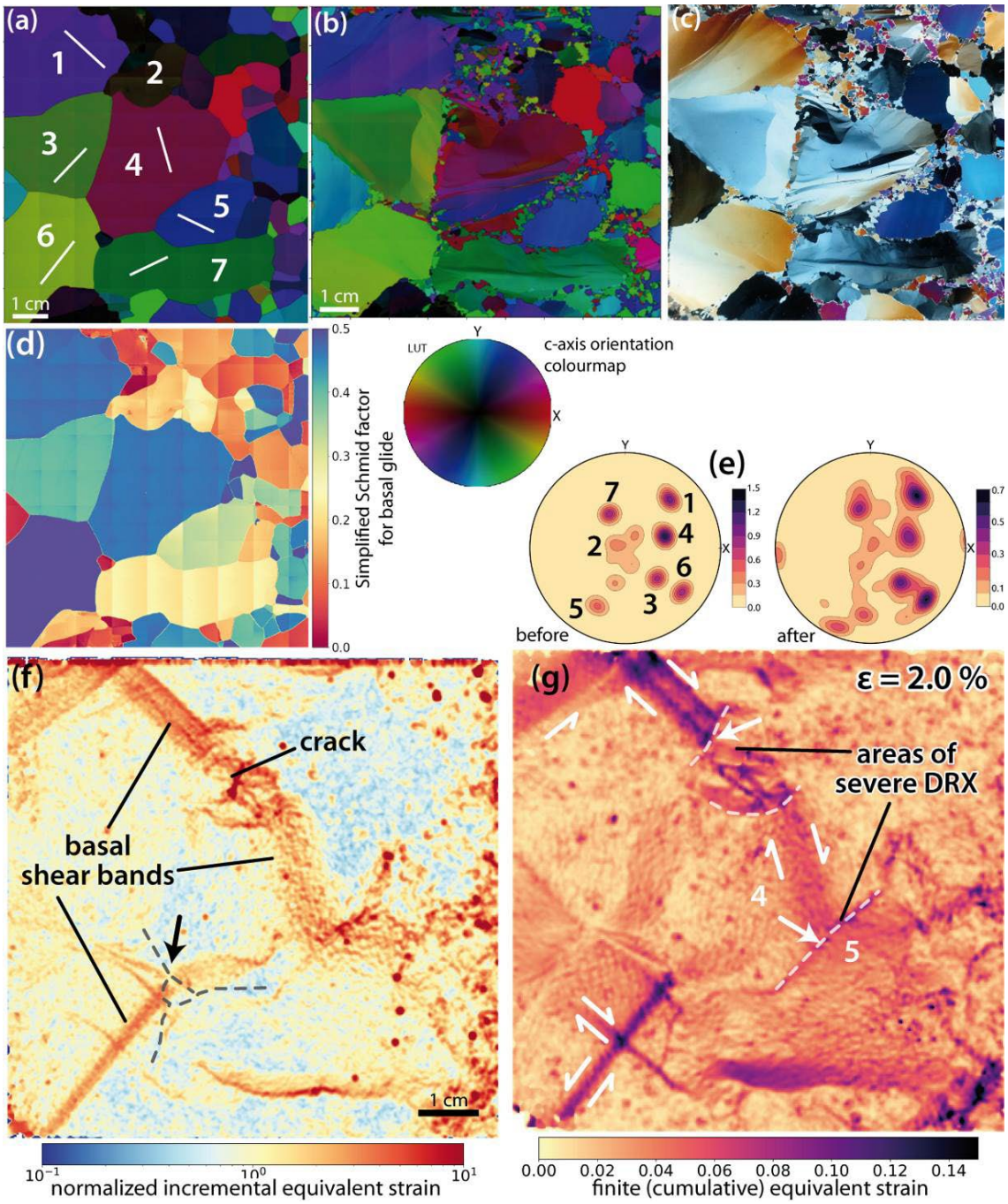

Figure 2. Microstructure, Schmid factor for basal glide, pre- and post-deformation CPO maps, and strain field at 2.0% bulk strain for sample A. (a, b) Pre- and post-deformation (9.5% bulk shortening) c-axis orientation maps. The projection of the basal planes onto the sample surface in the numbered grains is

indicated by white lines in (a). (c) Post-deformation cross-polarized light image (d) Schmid factor map for basal glide according to initial crystal orientations. Note that grains #1, #4, #6 have high Schmid factors (c-axis at ~45–73º to the compression normal), whereas grain #2 and #7 have moderate to low Schmid factors. (e) Pre- and post-deformation contoured c-axis pole figures with orientations. Upper hemisphere equal-area projections. (f) Normalized incremental Von Mises (2D) equivalent strain at 2.0% of bulk strain. Basal shear bands, the location of the crack produced at 1.4 % of shortening and a few grain boundaries are indicated. The black arrow indicates an example of slip transfer across a grain boundary (from grain #6 to #4). (g) Finite (cumulative) Von Mises 2D equivalent strain at 2.0% of bulk strain. The white dashed lines and arrows indicate a few selected grain boundaries that act as barriers to the dislocation motion of the basal shear bands. Note that these are the zones with severe development of dynamic recrystallization.

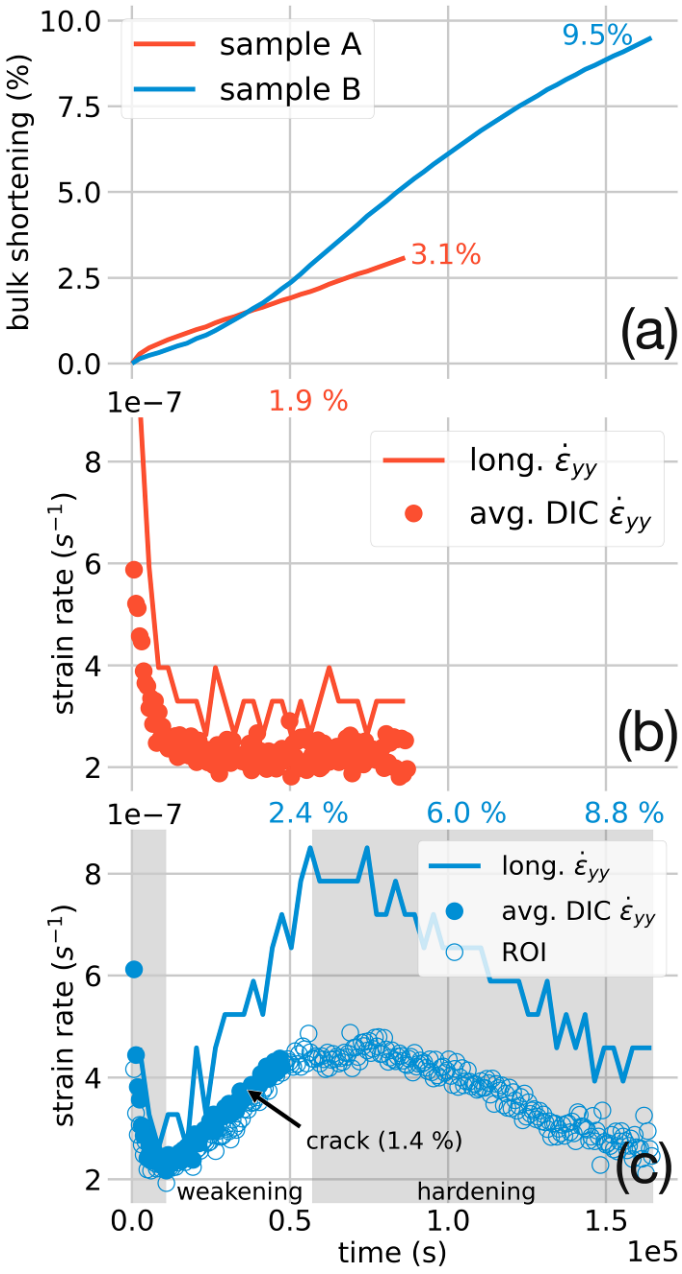

Figure 3. Evolution of strain and strain rate over time. For comparison, the time scale is the same in all plots. (a) Creep curves for samples A and B. Bulk shortening represents the finite longitudinal (engineering) strain parallel to the shortening axis. (b) Strain rate evolution of sample A determined via evolution with time of the finite longitudinal strain (line) and digital image correlation using the variation of the average (median) strain in the vertical direction σ_{yy} (markers). After a short primary creep, ~0.9 %, sample A experienced steady-state creep up to 3.1%. (c) Strain rate evolution of sample B. Due to the degradation of the speckle pattern quality with time, DIC-derived strain rates were estimated over the whole area only up to 2.4 %. Focusing on a region of interest (ROI) where the speckle pattern preserved a good quality (this ROI corresponds to the one shown in figure 4), we also determined the strain rates to completion (hollow markers). After a short primary creep (~0.4 %), sample B underwent an accelerated creep stage (weakening) up to ~2.9% and a deceleration creep stage (hardening) to completion at 9.5%. The different creep stages are highlighted by shaded areas. The equivalence between time and finite longitudinal strain is given at selected points for both samples at the top (in colour). The time at which the crack occurs in sample B is also indicated.

The macroscopic mechanical evolution of sample B, shortened up to 9.5%, is markedly different (Fig. 3a, c). Sample B had a faster primary creep stage with a decrease in strain rate down to ~2.5×10^{-7} s^{-1} at ~0.4% of bulk shortening. However, sample B displayed no steady-state behaviour. Primary creep was followed by an increase in longitudinal strain rate (weakening) up to ~8×10^{-7} s^{-1} at ~2.9% bulk shortening and then by a decrease in strain rate (hardening) until the end of the experiment down to a longitudinal strain rate of ~4.6×10^{-7} s^{-1} at 9.5% bulk shortening. The variation of the average (median) (σ_{yy}) strain rate over time estimated from DIC follows a similar trend even when the DIC strain is estimated over a smaller region that retained an acceptable quality speckle pattern (Fig. 3c), thus validating the DIC data in such region up to 9.5%.

3.3 Comparison between the strain field evolution from DIC and the microstructure

Both samples showed an initial transient stage in which strain localised nearby grain boundaries (at a scale of hundreds of microns or smaller). In this stage, incremental equivalent strains 5 to 10 times higher than the average occurred in the vicinity of virtually all grain boundaries (Figs. 4, 5 and 6). In-plane rotation maps indicate that this strain localisation along grain boundaries often has a simple shear component (Fig. 4). Analysis of the DIC data for this early stage in sample B also reveals that some shear bands started to propagate from triple junctions (arrows in Fig. 4). Strain localisation vanished along most grain boundaries at a longitudinal shortening of less than 0.2 % (i.e. at primary creep) (Figs. 5 and 6; see also movies A2 and B2 in Supplementary Material) in both samples. The transient stage in sample B was followed by a short period of almost homogeneous deformation up to a bulk strain of ~0.4% (Fig. 6 and movie B2 for a full sequence). DIC data show strain localised in a few shear bands, with apparent widths ranging from 1 to 8 mm, which grew until they coalesced to form an almost continuous system crosscutting the entire sample (Figs. 1, 2, 5 and 6). The exact evolution of the strain field differs, however, between the two samples.

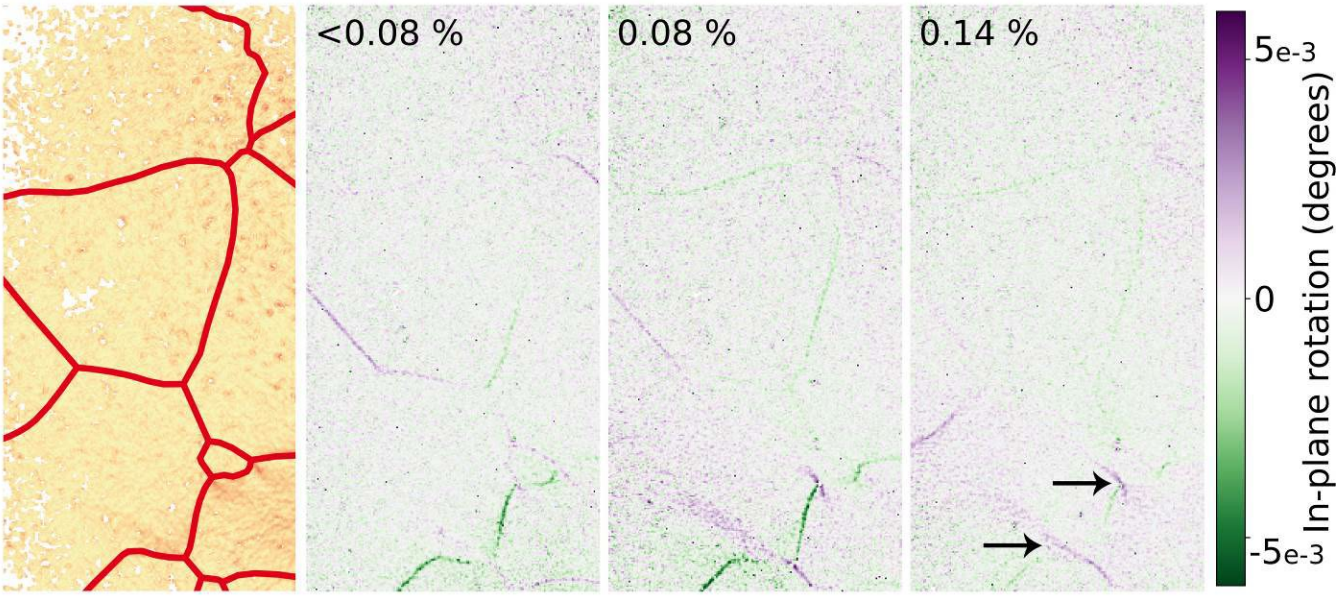

Figure 4. Example of the initial transient deformation stage in a region of interest of sample B. At left, raw equivalent strain map with delineated initial grain boundaries for reference. The sequence shows how strain localised and delocalised quickly at grain boundaries using in-plane rotation maps; purple and green colours indicate clockwise and counter-clockwise shear senses, respectively. The complete initial transient stage for both samples is in the Supplementary material.

Sample A

As previously described, almost 1/3 of sample A was composed of two very coarse grains (#1 and #2) with low to moderate (0-0.25) Schmid factors. DIC-derived strain maps indicate that these grains accommodated most of the imposed deformation. Strain localisation started early, already at 0.1% bulk shortening, at two sites. The first is the lower segment of the grain boundary between grains #1 and #2, which was the only grain boundary preserving strain localisation at the end of the initial transient stage (Figs. 1f, g and 5). Strain continued to accumulate at this interface until the end of the experiment, but its intensity varied in time and space along the grain boundary and the strain localisation along the boundary decreased during the experiment (Fig 5; see movie A2 in Supplementary Material). Most dynamic recrystallization occurred along this grain boundary (Fig. 1b, c). Strain localisation also propagated from a place with a sharp variation in the orientation of this grain boundary into grain #2 forming a slightly curved non-basal band with a diffuse end (Figs. 1f, g and 5). A shear band with a similar orientation also developed in grain #2 starting from the left edge of the sample. Strain localisation in the non-basal bands was accompanied by the formation of subgrains, kinks, and, in the curved one, dynamic recrystallization (Fig 1c).

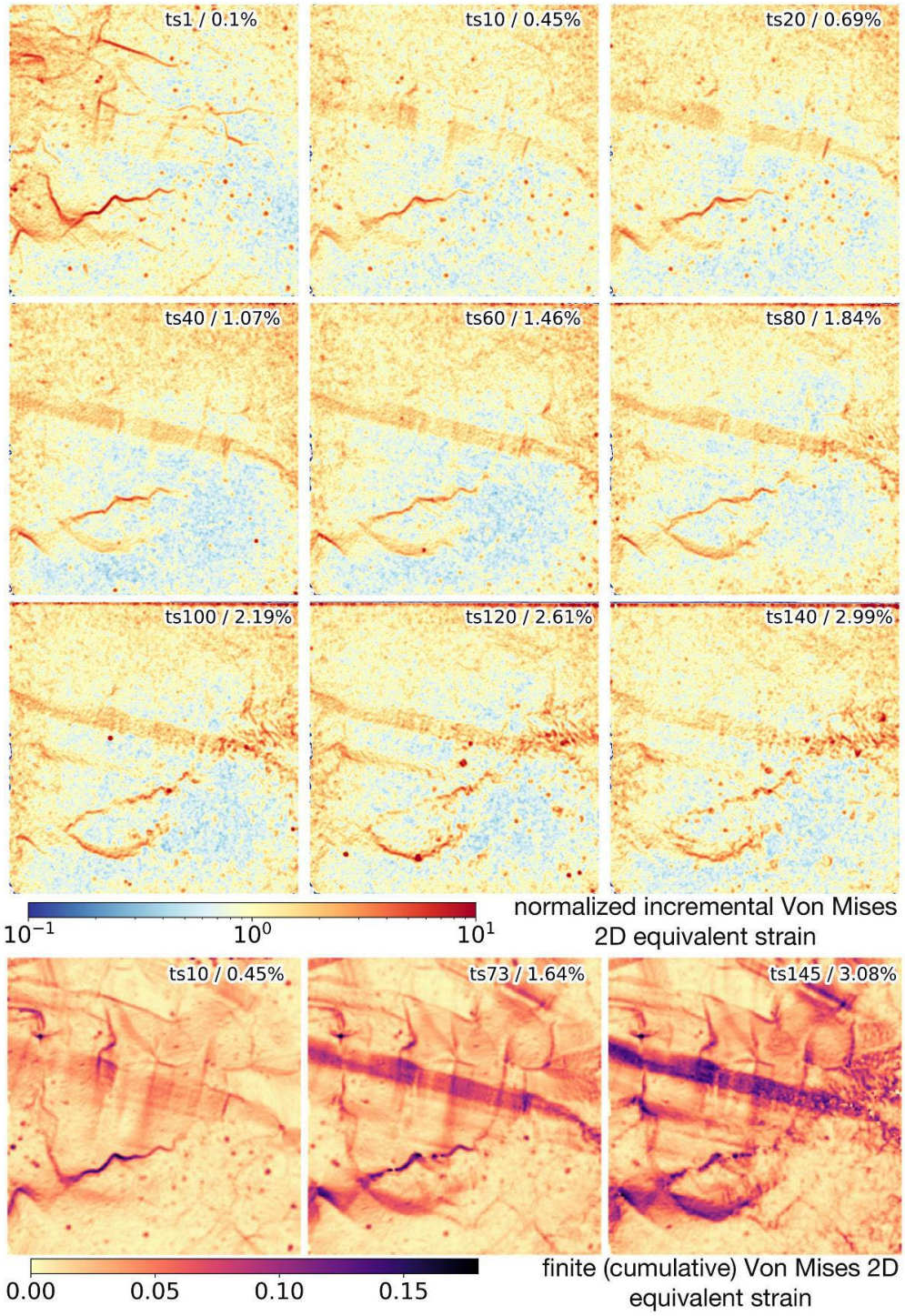

Figure 5. Selected frames of the sequence of incremental (estimated every 10 minutes of creep) and finite equivalent 2D strain evolution of sample A (for the complete sequence see movie A2 in Supplementary material). For reference, the time step (ts), i.e. the image number within the correlation sequence, and percentage of bulk longitudinal shortening are indicated in the top left.

In parallel, a ~7 mm wide shear band developed within grain #1 parallel to its basal plane at a high angle (77.5°) to the imposed shortening (Figs. 1f, g and 5). Already at 0.28% of bulk shortening, this shear band crosscut the entire grain and propagated into the neighbouring grains (~1.5–4 mm wide), affecting the entire sample width. The orientation of the shear band parallel to the basal plane of crystal #1 indicates that most deformation was accommodated by basal slip despite the moderate Schmid factor of the grain (~0.2, see Fig. 1d). The shear band is on average thinner in the neighbouring grains where non-basal shear bands were developed. Transient (at bulk shortenings between 0.28-1%) strain localisation occurred at the intersection between the band and the boundary of grain #1 on the right, which is another site with severe development of dynamic recrystallization (cf. Figs. 1f, g and 5). Strain concentration at this boundary decreased with the propagation of the shear band into the neighbouring grains up to the free surface of the sample (see movie A2 in Supplementary Material). Within grain #1, this shear band produced neither dynamic recrystallization nor significant dislocation substructures, remaining invisible in the optical image and the crystallographic orientation map (cf. Figs. 1cb, c *vs.* f, g). From ~1.8 % bulk shortening onwards, a slightly thinner basal shear band developed in this same grain spaced from the first one by ~1 cm. It did not propagate into neighbouring grains but produced some strain localisation and limited recrystallization at its interception with the boundary of grain #1 on the left (see movie A2 in Supplementary Material).

Sample B

After the initial transient stage, DIC data show that strain in sample B was mostly accommodated in a few mm-wide (apparent thicknesses vary between 3 and 7.5 mm) intragranular shear bands oblique (13° to 45?) to the compression (Figs. 2f, g and 6). Macroscopically, this corresponds to the weakening stage evidenced by the increase in strain rate over time (Fig. 3c). Shear bands mainly developed in coarse grains with high Schmid factors (>0.4) following the orientation of the basal plane, specifically in grains #1, #4 and #6 (cf. Figs. 2a *vs* f, g). There are, however, a few shear bands that do not follow basal planes. In particular, those developed in grains #1 and #6 perpendicular to the basal planes (Fig. 2f) and the one in grain #7, which is linked to a kink band. In grain #6, the non-basal shear bands nucleated already in the transient stage from a triple junction (Fig. 4). These non-basal shear bands are thinner (in grain #6) or less marked (in grain #1) than the basal ones.

Strain localisation started at multiple sites within the sample and the shear bands propagated unevenly across the sample. The DIC sequence shows that the formation of shear bands started as early as 0.14% of bulk shortening in the lower part of the sample (Fig. 4). The basal shear band affecting grain #6 propagated from the triple junction between grains #6, #4, and a tiny grain with a very low Schmid factor value located between grains #4, #6, and #7 at a bulk shortening ~0.5% and evolved fast crosscutting the entire grain at a bulk shortening ~0.7% (Fig. 6 and movie B2 in Supplementary material). Strain localisation became progressively stronger within it and at bulk shortenings ~1.4 % this shear band propagated into grain #4 (Fig. 6).

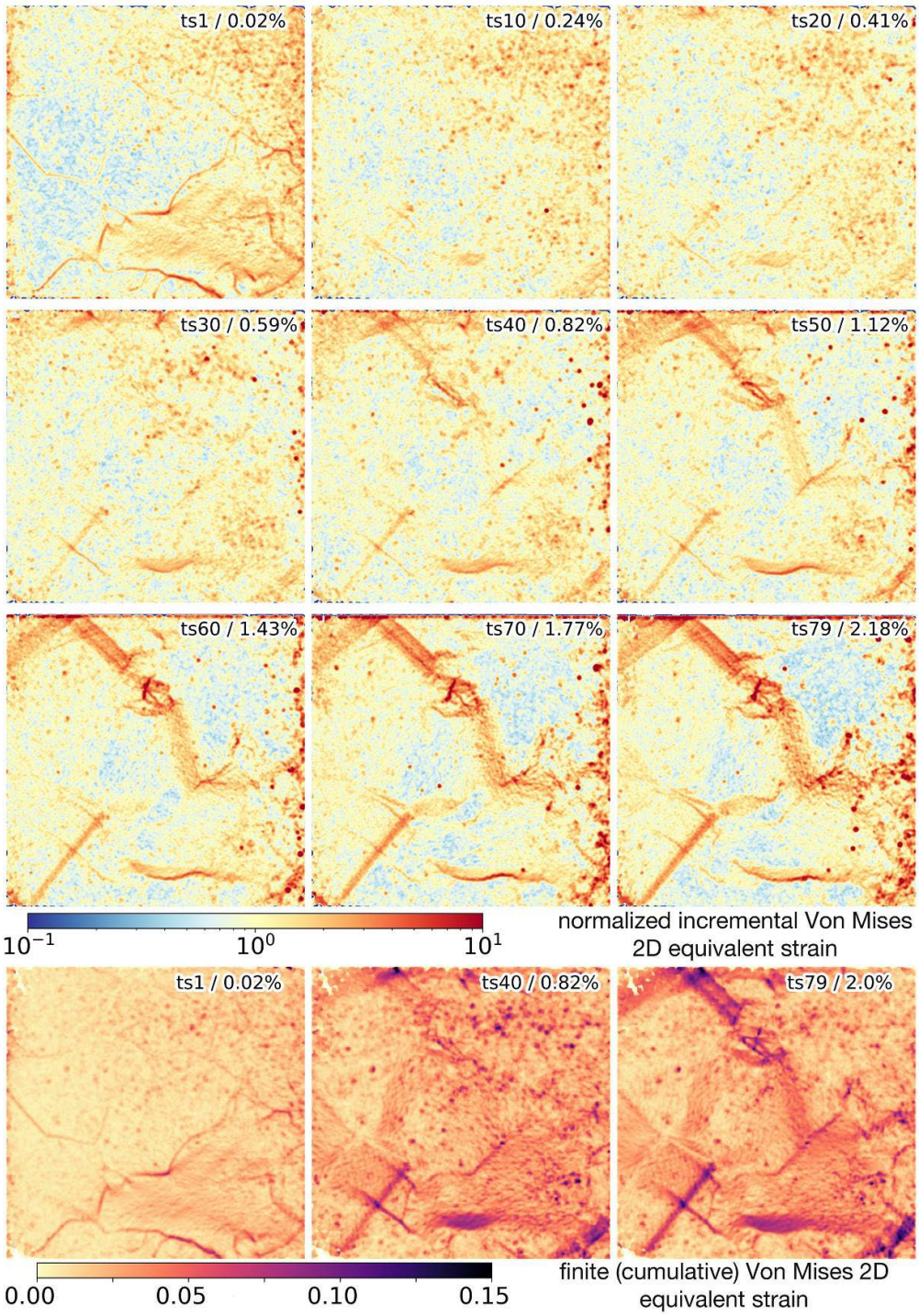

Figure 6. Selected frames of the sequence of incremental (estimated every 10 minutes of creep) and finite equivalent 2D strain evolution of sample B (for the complete sequence see movie B2 in Supplementary material). For reference, the time step (ts), i.e. the image number within the correlation sequence, and percentage of bulk longitudinal shortening are indicated in the top left.

The best-developed shear band in this sample propagated with a basal orientation from the top of the sample into grain #1 (at a bulk shortening of 0.73 % see movie B2), continued into grain #2 as a non-basal deformation band with a fuzzy strain distribution, and propagated into grain #4 as a basal shear band (bulk shortening of ~0.8 %) (Figs. 2f, g and 6; see also movie B2). The deformation band finally stalled at the grain boundary between grains #4 and #5, producing a marked strain concentration along this grain boundary (Figs. 2f, g and 6). A diffuse build-up of strain in grain #5 connected the two shear zones, producing a strain localisation network that crosscut the whole sample. Within grain #2, the propagation of the shear band was accompanied by the development of a crack normal to the shear band elongation at a bulk shortening of 1.4% (Figs. 1f, 5 and movie B2).

Regarding the links between the strain field from DIC and microstructures, basal-slip shear bands remain mostly invisible inside the grains in the polarised optical image and crystallographic orientation maps, whereas non-basal strain localisation bands have a clear signature in the microstructure in the form of strong orientation gradients, kink bands, or dynamic recrystallization (Figs. 1 and 2 and movies A2 and B2 in Supplementary material). Grains #1, #4 and #6 deformed mainly through basal-slip shear bands developing a notable change in shape during deformation, consistent with the high strain they accumulated. There is a correlation between the zones where the shear bands propagation stall and the generation of severe dynamic recrystallization. Three areas in sample B display severe recrystallization (Fig. 2b, c *vs* g). One is the boundary between grains #4 and #5, where the basal shear band in grain #4 stalled due to the strong misorientation between the two grains. The other corresponds to grain #2, a grain with a very low Schmid factor that serves as a strain transfer zone between the basal shear bands of grains #1 and #4. The development of a small crack in grain #2 at ~1.4 % bulk shortening indicates that it supported high local stresses even if the bulk sample was weakening, as indicated by the increase in bulk strain rate (Fig. 3c). The last severe recrystallization domain links the diffuse deformation in grain #5 to the sample edge. On the other hand, although many non-basal strain localisation bands are associated with kink bands, not all kink bands are sites of significant long-lasting strain localisation (e.g. kink bands in grain #4 of sample B, Fig. 2).

Lastly, comparison of the average finite strain derived from DIC and the initial Schmid factor for basal slip for a few coarse grains in both samples shows that the two parameters are uncorrelated (Fig. 7). This explicitly indicates that the local stress field strongly deviates from the macroscopic one due to interactions between neighbouring grains.

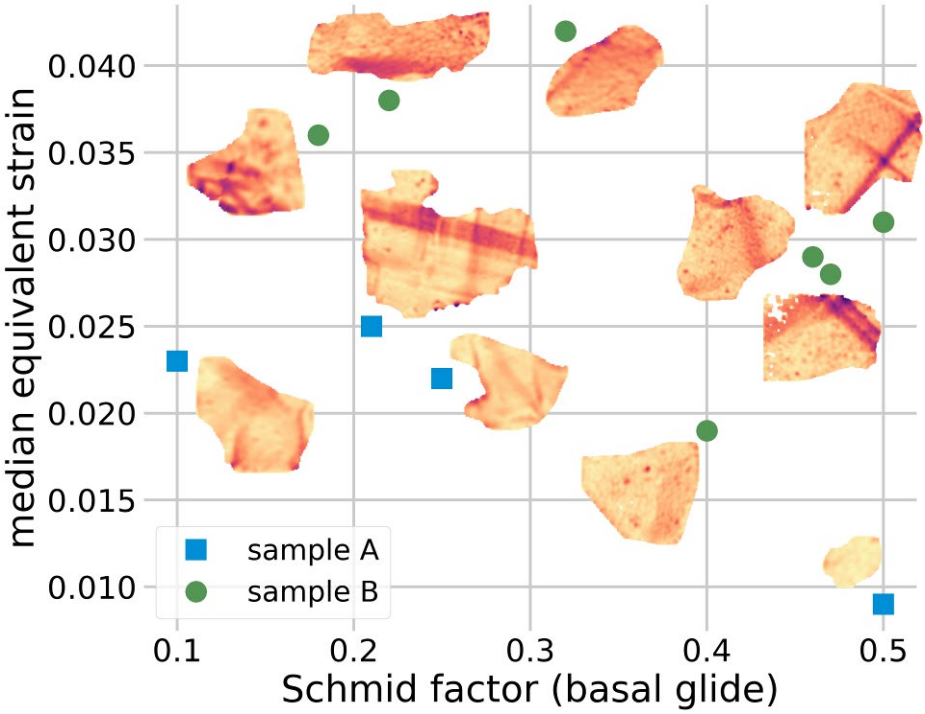

Figure 7. Schmid factor vs average (median) equivalent finite strain for 2 % bulk shortening for different grains of samples A and B. Note the lack of trend between the two variables. Grains are not represented at the same scale. Colour maps indicate cumulative equivalent strain up to 2% bulk shortening.

3.4 Comparison between full-field simulations and observations

The full-field simulations do not capture the initial transient strain localisation nearby grain boundaries observed in the two examples at small bulk shortening (<0.2%). For larger strains, the simulation predicts correctly the location of the basal shear band within grain #1 in sample A (Fig. 8). It also forecasts correctly the development of non-basal shear bands in grain #2. The main discrepancy between the predicted strain field and that derived from DIC is the lack of strain localisation nearby the grain boundary between grains #1 and #2. For sample A, high work rate values in the simulation correlate well with the location of the shear bands that crosscuts the entire sample and with areas that developed severe dynamic recrystallization in the experiment (cf. Figs. 1 and 8).

For sample B, the full-field simulation is unable to predict any of the three shear bands that accommodated most of the deformation (Fig. 8). This discrepancy is probably due to strong local reorientations of the microstructure that occurred at low strains in the experiments. For example, the simulation predicts high prismatic slip activity in grain #4, while orientation maps, optical images, and DIC data show the development of kink bands and significant activation of basal glide in this grain. There is also no clear correlation between high work rates areas in the simulations and those with severe recrystallization in the experiments (cf. Figs. 2 and 8). The simulation, however, predicts properly the non-basal shear band developed in grain #6 (Fig. 8).

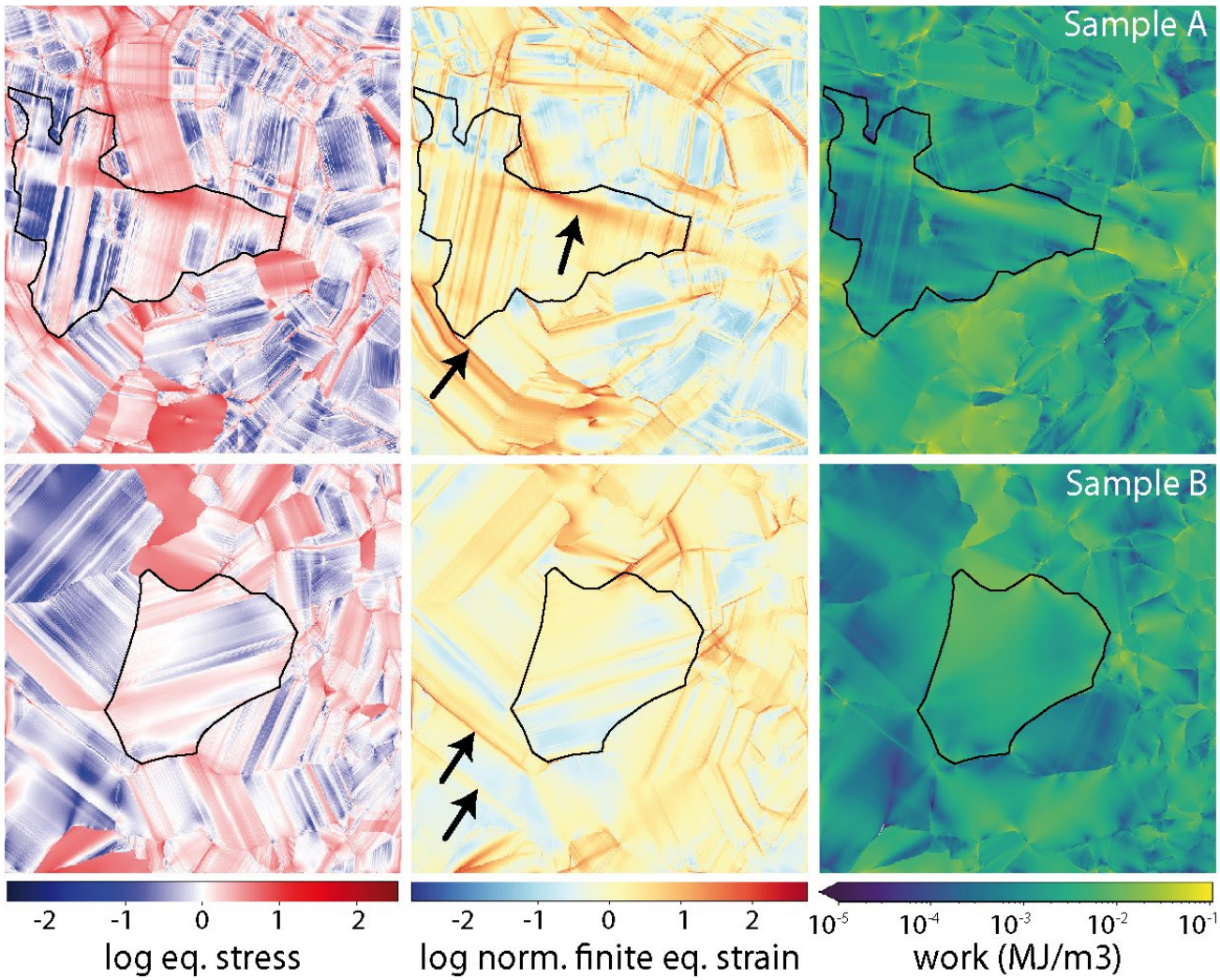

Figure 8. Full-field simulation maps for normalized stress, normalized strain, and plastic work (the product of strain rate and stress). The simulated fields correspond to a longitudinal shortening of 0.5%. Two grains are delineated to facilitate comparison with maps estimated from DIC data. Arrows on the strain maps indicate zones of strain localization observed in the experimental data.

4. Discussion

Although the samples are not representative volume elements given their coarse grain size relative to the sample dimension, both high-temperature creep tests share several common features. The most striking observation when comparing the evolution of the strain field and that of the microstructure is the decoupling between strain localisation and the development of microstructures linked to the accumulation of geometrically necessary dislocations, such as crystal lattice distortion, recrystallization, or the development of kink bands. The most effective strain localisation, well-recorded by DIC, occurred through intracrystalline shear bands parallel to the basal planes of the crystals leaving hardly any lattice distortion (intragranular misorientation) or

dynamic recrystallization within the grains. Despite the lack of severe intracrystalline lattice distortion exhibited by some of these grains, all grains affected by basal shear bands show a severe change in shape. This strain at grain scale might only be quantified if the initial state is known, which rarely occurs in nature, or by using in situ observational techniques such as DIC.

Dynamic recrystallization occurred mainly nearby grain boundaries and triple junctions, as in previous studies (Chauve et al., 2015; Piazolo et al., 2015), but it was best developed at the boundaries that hinder the transfer of dislocation motion associated with basal slip between grains (e.g. at the interface between grains #4 and #5 in Fig. 2). The intensity of recrystallization appears to be proportional to the strain incompatibility between neighbouring grains which results in local stress and strain concentration. Development of recrystallization (or cracks at higher strain rates, see Chauve et al., 2017) allows to relax the incompatibility. Comparison between full-field simulations and the experimental observations for sample A suggests that dynamic recrystallization develops in places where the work rate, the product of strain rate and stress, was high. However, not all high work rate areas in the simulation developed recrystallization, indicating that although a high work rate is most likely required for triggering recrystallization there are other factors at play.

Full-field simulations were unable to reproduce the formation of the main basal shear bands for sample B, most likely because of the early development of kinks in grains #4 and #7 that could not be modelled, invalidating the predicted stress and strain fields for bulk strains as low as 0.5%. Another notable mismatch between the full-field simulations and the experimental observations is that the former does not foresee the transient localisation of strain nearby grain boundaries at low bulk strains ($<< 0.2$ %). This transient probably reflects the initial development of the strain field in which grain boundaries act as barriers to dislocation movement, concentrating dislocation pile-ups in their vicinity and producing local strain as hypothesised by Duval et al. (1983).

The DIC and crystal orientation data presented here agree with the large body of evidence that creep deformation on single-grain and polycrystalline ice mainly proceeds by dislocation glide on basal planes (Duval et al., 1983; Weertman, 1983). Most of the deformation accommodated by basal slip, however, remains undetectable to observations based on intracrystalline misorientation (e.g. AITA, EBSD) and intracrystalline lattice distortion (i.e. GNDs). This means that the relative occurrence of dislocation types that form subgrains does not gauge the relative contribution of slip systems that accommodate strain neither at the grain nor the macroscopic scale. This view solves the paradoxical observation of non-basal dislocations contributing to up to 35-40% of the total intracrystalline misorientation in ice polycrystals measured with high spatial resolution cryo-EBSD mapping and X-ray Laue diffraction (Chauve et al. 2017; Weikusat et al. 2017). A similar conclusion has recently been proposed in a study focusing on how dynamic recrystallization by subgrain rotation develops in olivine polycrystals, another low-symmetry crystalline material with strong viscoplastic anisotropy (Lopez-Sanchez et al., 2021). A similar conclusion was hinted in a previous study based on an apparent contradiction between olivine crystal preferred orientations and intragranular misorientation data (Soustelle et al. 2010). The present study puts tighter constraints on this phenomenon by combining DIC and crystal orientation data.

The present observations are also consistent with those from a recent study coupling high-resolution (*nm* scale) DIC and crystal orientation mapping through electron backscatter diffraction (EBSD) in a nickel (cubic) superalloy deformed to 2% (Harte et al. 2020). This study revealed: (1) a strong correlation between active slip systems and the Schmid factor, but no or weak correlation between the Schmid and Taylor factors and the finite plastic strain accommodated by the crystal (see Grennerat et al. 2012 for a similar conclusion in ice) and (2) no correlation between the overall plastic strain experienced by a grain and its average lattice misorientation, especially when only one slip system is active. The present study extends these observations and the related conclusions to materials with lower symmetry and higher viscoplastic anisotropy. This is the case with ice, but also with all major rock-forming minerals, like olivine, pyroxenes, or quartz. The present observations document that basal glide in Ih ice at high homologous temperatures can proceed in an unimpeded manner without producing dislocation substructures that increase local misorientation. Similar unimpeded glide, characterized by extreme elongation of crystals without recrystallization, is observed in olivine, quartz, or orthopyroxene crystals when they are oriented to deform by dislocation glide in their easiest slip system. High strains with no development of subgrains have also been observed in single crystal deformation experiments when olivine is oriented to activate solely the [100](010) system (Tielke et al. 2019). Altogether these data imply that misorientation-based proxies –such as GOS, KAM or average subgrain misorientation – do not gauge the total plastic strain at the grain scale and therefore caution should be applied when using such proxies to estimate the bulk strain (e.g., Hughes et al., 1998; Pennock and Drury, 2003) or strain intensity at local scales. Even if a proportional relationship exists between the bulk strain and the average misorientation over representative elementary volumes, it would be necessary to check how different initial microstructural parameters (e.g. grain size, CPO) might affect this proportionality to set a reliable universal approximation.

5. Conclusion

The present combination of DIC and orientation data documents the decoupling between the strain intensity and its imprint on the microstructure via the development of dislocation substructures (misorientation gradients, subgrains, or kinks). The decoupling results from a highly efficient strain accommodation by basal glide that proceeds essentially unimpeded at the grain scale, leaving no imprint in the final microstructure. These conclusions can be extrapolated to any highly anisotropic crystalline material showing few slip systems with contrasted critical resolved shear stresses, including all major rock-forming minerals (olivine, quartz, pyroxenes, micas, etc.) and hexagonal metallic alloys. The present results explain the apparent contradiction between the relative activity of slip systems inferred from crystal preferred orientation data or mechanical tests and that inferred from intragranular misorientation data previously observed in ice and other rock-forming minerals. They also document that misorientation data is an unreliable gauge of the contribution of the different slip systems to deformation. The present study also validates that dynamic recrystallization plays a role in the feedback between the strain field and the microstructure evolution, accommodating strain incompatibility and reducing local stress concentrations. However, under the studied conditions, grain size reduction by dynamic

recrystallization is a consequence rather than a driver for strain localisation. The decoupling between strain localization and microstructural evolution documented in this study should be integrated into models for predicting strain localization as a function of the evolution of microstructural parameters, like grain size reduction by recrystallization or dislocation distribution.

Acknowledgements. This work was supported by a postdoctoral fellowship co-funded by the European Union and the Government of the Principality of Asturias (Spain) [grant number ACA17-32] within the Marie Skłodowska-Curie COFUND Actions FP7 to MALS and by the European Research Council (ERC) under the European Union's Horizon 2020 Research and Innovation programme [grant agreement No 882450 – ERC RhEoVOLUTION].

Appendix A. Digital image correlation data treatment

DICe software provides different algorithms for digital image correlation. We used the *feature matching* algorithm for the initialization, a *gradient-based method* for optimization, and the *Keys cubic* method (Keys, 1981) for interpolation (see metadata in Supplementary material). For some specific sequences of interest, we also used the *simplex* algorithm for optimization, as it produces a better coverage at the cost of a much longer time to correlate the images. The formulation used to compute the displacement and strain full-fields from digital image sequences is detailed in Turner (2018, 2016). During image correlation, subsets with the sum of a square of subset intensity gradients (SSSIG) proxy (Pan et al., 2008) above 150 were discarded, this ultimately produces a few missing values within the strain maps but correlation coverage remains above 99% in all cases.

To visualize variations in the strain intensity, we used the Von Mises 2D equivalent strain (see equation 1) and in-plane rotation maps that plot the rotational component of the 2D strain. DIC strain estimate can include elastic and plastic components without distinction. We assumed that the elastic part for a stress of 0.5 MPa in ice is negligible, i.e. with Young's modulus of 9.1 GPa which implies $\varepsilon_{elastic} \ll \varepsilon_{plastic}$, and thus all the measured strain is considered plastic/viscoplastic. The quality of the DIC solution and the floor noise (maximum expected precision) for the displacement and strain (VSG) gauges were calculated by comparing the images acquired in the undeformed state under the same environmental conditions and using the same displacement and strain parameters to analyse the deformed sequence.

Samples suffered from speckle quality degradation with time, including speckle tearing at high finite strains in sample B (see movie B1 in Supplementary Material). These issues were overcome by: (1) using incremental image correlation, which complied with one of the central goals of the study that was to track the evolution of the incremental strain with time, (2) focusing the study on regions where the random speckle pattern was better preserved over time, and (3) reconstructing the maps using convolution (interpolation) algorithms to replace missing data and remove noise based on neighbour's values. For convolution, we used the Python Astropy module v4.2.1 (Robitaille et al., 2013) with a Gaussian kernel (see Supplementary Material). We also performed finite correlations for specific deformation stages and individual grains. In these cases, we increased the subset and the VSG size to 45 x 45 pixels and the step size to 15 pixels to improve coverage and strain accuracy at the cost of losing spatial resolution. General post-processing procedures can be consulted in https://github.com/marcoalopez/Jupyter4DICe.

Out-of-plane specimen deflections were checked after deformation. For sample A (bulk shortening of 3.1 % after 24h:10min), most of the surface remained flat excepting a small area in the upper left corner related to the development of a shear band. For sample B (shortening of 9.5% after 45h:50min), the final surface was wavy with out-of-plane displacements of up to a few mm (see Supplementary Material). Based on previous experiments under similar conditions (Chauve et al., 2015), we expect that the surface remained fairly flat up to ~5% bulk shortening. Yet, strain maps for the entire surface of sample B were limited to a maximum bulk strain of 2% due to speckle degradation.

References

Chauve, T., Montagnat, M., Lachaud, C., Georges, D., Vacher, P., 2017b. Strain field evolution at the ductile-to-brittle transition: a case study on ice. Solid Earth 8, 943–953. https://doi.org/10.5194/se-8-943-2017

Chauve, T., Montagnat, M., Piazolo, S., Journaux, B., Wheeler, J., Barou, F., Mainprice, D., Tommasi, A., 2017a. Non-basal dislocations should be accounted for in simulating ice mass flow. Earth Planet. Sci. Lett. 473, 247–255. https://doi.org/10.1016/j.epsl.2017.06.020

Chauve, T., Montagnat, M., Vacher, P., 2015. Strain field evolution during dynamic recrystallization nucleation; A case study on ice. Acta Mater. 101, 116–124. https://doi.org/10.1016/j.actamat.2015.08.033

Dong, Y.L., Pan, B., 2017. A Review of Speckle Pattern Fabrication and Assessment for Digital Image Correlation. Exp. Mech. 57, 1161–1181. https://doi.org/10.1007/s11340-017-0283-1

Duval, P., Ashby, M.F., Anderman, I., 1983. Rate-controlling processes in the creep of polycrystalline ice. J. Phys. Chem. 87, 4066–4074. https://doi.org/10.1021/j100244a014

Grennerat, F., Montagnat, M., Castelnau, O., Vacher, P., Moulinec, H., Suquet, P., Duval, P., 2012. Experimental characterization of the intragranular strain field in columnar ice during transient creep. Acta Mater. 60, 3655–3666. https://doi.org/10.1016/j.actamat.2012.03.025

Harte, A., Atkinson, M., Preuss, M., Quinta da Fonseca, J., 2020. A statistical study of the relationship between plastic strain and lattice misorientation on the surface of a deformed Ni-based superalloy. Acta Mater. 195, 555–570. https://doi.org/10.1016/j.actamat.2020.05.029

Hughes, D.A., Chrzan, D.C., Liu, Q., Hansen, N., 1998. Scaling of Misorientation Angle Distributions. Phys. Rev. Lett. 81, 4664–4667. https://doi.org/10.1103/PhysRevLett.81.4664

International Digital Image Correlation Society, Jones, E.M.C., Iadicola, M.A. (Eds.), 2018. A Good Practices Guide for Digital Image Correlation. https://doi.org/10.32720/idics/gpg.ed1

Keys, R., 1981. Cubic convolution interpolation for digital image processing. IEEE Trans. Acoust. Speech Signal Process. 29, 1153–1160. https://doi.org/10.1109/TASSP.1981.1163711

Lopez-Sanchez, M.A., Tommasi, A., Ismail, W.B., Barou, F., 2021. Dynamic recrystallization by subgrain rotation in olivine revealed by electron backscatter diffraction. Tectonophysics 815, 228916. https://doi.org/10.1016/j.tecto.2021.228916

Moulinec, H., Suquet, P., 1998. A numerical method for computing the overall response of nonlinear composites with complex microstructure. Comput. Methods Appl. Mech. Eng. 157, 69–94. https://doi.org/10.1016/S0045-7825(97)00218-1

Pan, B., Xie, H., Wang, Zhaoyang, Qian, K., Wang, Zhiyong, 2008. Study on subset size selection in digital image correlation for speckle patterns. Opt. Express 16, 7037–7048. https://doi.org/10.1364/OE.16.007037

Pennock, G.M., Drury, M.R., 2005. Low-angle subgrain misorientations in deformed NaCl. J. Microsc. 217, 130–137. https://doi.org/10.1111/j.1365-2818.2005.01410.x

Peternell, M., Russell-Head, D. s., Wilson, C. j. l., 2011. A technique for recording polycrystalline structure and orientation during in situ deformation cycles of rock analogues using an automated fabric analyser. J. Microsc. 242, 181–188. https://doi.org/10.1111/j.1365-2818.2010.03456.x

Piazolo, S., Montagnat, M., Grennerat, F., Moulinec, H., Wheeler, J., 2015. Effect of local stress heterogeneities on dislocation fields: Examples from transient creep in polycrystalline ice. Acta Mater. 90, 303–309. https://doi.org/10.1016/j.actamat.2015.02.046

Robitaille, T.P., Tollerud, E.J., Greenfield, P., Droettboom, M., Bray, E., Aldcroft, T., Davis, M., Ginsburg, A., Price-Whelan, A.M., Kerzendorf, W.E., Conley, A., Crighton, N., Barbary, K., Muna, D., Ferguson, H., Grollier, F., Parikh, M.M., Nair, P.H., Günther, H.M., Deil, C., Woillez, J., Conseil, S., Kramer, R., Turner, J.E.H., Singer, L., Fox, R., Weaver, B.A., Zabalza, V., Edwards, Z.I., Bostroem, K.A., Burke, D.J., Casey, A.R., Crawford, S.M., Dencheva, N., Ely, J., Jenness, T., Labrie, K., Lim, P.L., Pierfederici, F., Pontzen, A., Ptak, A., Refsdal, B., Servillat, M., Streicher, O., 2013. Astropy: A community Python package for astronomy. Astron. Astrophys. 558, A33. https://doi.org/10.1051/0004-6361/201322068

Soustelle, V., Tommasi, A., Demouchy, S., Ionov, D.A., 2010. Deformation and fluid-rock interaction in the supra-subduction mantle: Microstructures and water contents in peridotite xenoliths from the Avacha volcano, Kamchatka. J. Petrol. 51. https://doi.org/10.1093/petrology/egp085

Suquet, P., Moulinec, H., Castelnau, O., Montagnat, M., Lahellec, N., Grennerat, F., Duval, P., Brenner, R., 2012. Multi-scale modeling of the mechanical behavior of polycrystalline ice under transient creep. Procedia IUTAM, IUTAM Symposium on Linking Scales in Computations: From Microstructure to Macro-scale Properties 3, 76–90. https://doi.org/10.1016/j.piutam.2012.03.006

Sutton, M.A., Orteu, J.-J., Scheirer, Hubert, 2009. Image Correlation for Shape, Motion and Deformation Measurements, 1st ed. Springer, Boston, MA.

Tielke, J., Mecklenburgh, J., Mariani, E., Wheeler, J., 2019. The Influence of Water on the Strength of Olivine Dislocation Slip Systems. J. Geophys. Res. Solid Earth 124, 6542–6559. https://doi.org/10.1029/2019JB017436

Turner, D. Z., 2018. An overview of the virtual strain gauge formulation in DICe (No. Sandia Report, SAND2018-5463 R).

Turner, D. Z., 2016. An overview of the gradient-based local DIC formulation for motion estimation in DICe (No. Sandia Report, SAND2016-7360 R).

Turner, D. Z., 2015. Digital Image Correlation Engine (DICe) Reference Manual, (No. Sandia Report, SAND2015-10606 O).

Weertman, J., 1983. Creep Deformation of Ice. Annu. Rev. Earth Planet. Sci. 11, 215–240. https://doi.org/10.1146/annurev.ea.11.050183.001243

Weikusat, I., Kuiper, E.-J.N., Pennock, G.M., Kipfstuhl, S., Drury, M.R., 2017. EBSD analysis of subgrain boundaries and dislocation slip systems in Antarctic and Greenland ice. Solid Earth 8, 883–898. https://doi.org/10.5194/se-8-883-2017

Wilson, C.J.L., Russell-Head, D.S., Sim, H.M., 2003. The application of an automated fabric analyzer system to the textural evolution of folded ice layers in shear zones. Ann. Glaciol. 37, 7–17. https://doi.org/10.3189/172756403781815401